Percolation transition in phase-separating active fluid

Monika Sanoria ⬤, Raghunath Chelakkot ⬤,[*] and Amitabha Nandi ⬤[†]

Department of Physics, Indian Institute of Technology Bombay, Powai, Mumbai 400076, India

The motility-induced phase separation exhibited by active particles with repulsive interactions is well known. We show that the interaction softness of active particles destabilizes the highly ordered dense phase, leading to the formation of a porous cluster which spans the system. This *soft limit* can also be achieved if the particle motility is increased beyond a critical value, at which the system clearly exhibits all the characteristics of a standard percolation transition. We also show that in the athermal limit, active particles exhibit similar transitions even at low motility. With these additional new phases, the phase diagram of repulsive active particles is revealed to be richer than what was previously conceived.

I. INTRODUCTION

Active matter systems consist of microscopic entities that consume chemical energy and convert it to mechanical motion [1–18]. Such systems display a variety of collective properties as a result of the interplay between the activity and the nature of interactions between the constituent entities [18–35]. Minimal theoretical models used to study the collective behavior of active matter belongs to two major categories. The first one involves purely alignment interaction between the active polar entities and leads to an emergence of global polar order [2,36–41]. The second class of models study the effect purely excluded volume interactions between the entities leading to a phase-separated state [21,22,35,42,43], known as motility-induced phase separation (MIPS). Unlike the systems with alignment interaction, the structural properties of the phase-separating systems have been so far known to be relatively simpler.

MIPS has received much attention during the last decade and have been studied extensively using particle-based simulations [22,42,43] and continuum descriptions [21,35,44]. The generic phase behavior for nearly hard particles with short-range repulsive interactions has been explored in some detail [22,42,43]. However, many of the dynamical properties, especially in the dense phase, are still being revealed [23,28,33]. Also, subtle modifications in the surrounding environment and the interparticle interactions lead to a range of intriguing collective properties [29,45–50], thus making such phase-separating systems still an interesting topic of research.

Numerical studies on MIPS have focused on systems where overlap distance between the particles are small but nonzero [22,45]. In such systems, an increase in motility causes a more compact hexatic packing of particles within the clusters, stabilizing the dense phase. On the other hand, it has also been shown that a higher degree of particle overlap leads to a destruction of MIPS as the particles can pass through each other [51]. But there lies an interesting regime where the overlap is significant while the particles still do not pass through. Such systems have been studied earlier in the equilibrium limit and were observed that a change in particle softness affects the high-density crystalline order [52,53]. Recent experiments with two-dimensional (2D) passive colloids have revealed that an increase in the particle softness causes complex self-assembled structures [54]. A natural question thus arises, whether such emergent complex structures are also possible for systems with soft active particles. This soft limit is particularly relevant since many active systems occurring in nature consist of deformable entities, for example, cells in tissues. Furthermore, since the numerical studies on phase separation have used soft particle models, it would be interesting to study the high-motility *soft* limit where the interparticle distances are small, to explore the possibilities of new phases beyond MIPS, and to obtain a complete understanding of their phase behavior.

Here we show that for a given particle softness, there exists a critical value of motility for soft active particles, beyond which the structurally ordered high-density cluster in MIPS becomes unstable, leading to the formation of porous, connected clusters which spans the system size. Our detailed analysis reveals that the transition to this connected state is caused by an interplay between motility and particle softness and shows all the characteristics of a standard percolation transition.

II. MODEL

Our numerical model consists of N active Brownian particles (ABPs), at position r_i with the direction of self-propulsion $\hat{\mathbf{n}}_i = (\cos\theta_i, \sin\theta_i)$ respectively, confined in 2D periodic boundary system of box length L. The dynamical equations of motion are given by the overdamped Langevin equation as [42]

$$\dot{\mathbf{r}}_i = \mu \sum_j \mathbf{F}(\mathbf{r}_{ij}) + v_p\hat{\mathbf{n}}_i, \tag{1}$$

$$\dot{\theta}_i = \xi_i^R. \tag{2}$$

---

[*]raghu@phy.iitb.ac.in

[†]amitabha@phy.iitb.ac.in

Here v_p is the self-propulsion speed and μ is the mobility. The Gaussian white noise ξ_i^R with mean zero and variance $2D_r$ satisfies the relation $\langle \xi_i^R(t) \xi_j^R(t') \rangle = 2D_r \delta_{ij} \delta(t - t')$, where D_r is the rotational diffusion coefficient. The repulsive force between a pair of particles is given as $\mathbf{F}(\mathbf{r}_{ij}) = k(\sigma - r_{ij})\hat{\mathbf{r}}_{ij}$; $r_{ij} < \sigma$ and zero otherwise. Here σ is the interaction diameter of the particle, k is the elastic constant that controls the stiffness of the particles, and $r_{ij} = |\mathbf{r}_i - \mathbf{r}_j|$. We use the nondimensional number $\text{Pe} = \frac{v_p}{\sigma D_r}$ (Péclet number) as a parameter to vary particle motility. We also define $\tilde{k} = \frac{\mu k}{D_r}$ as the nondimensional effective stiffness parameter. We keep $D_r = 0.005$, $\mu = 1$, $\sigma = 1$, while varying k from 5 to 40. We also vary Pe from 0 to 3000 and N from 3649 to 233 546. The integration time step $\Delta t = 10^{-3}$. The packing fraction $\phi = \frac{N\pi \sigma^2}{4L^2}$ varies from 0.1 to 0.8.

III. RESULTS

To quantify the phase behavior systematically, we calculate two quantities which characterize macroscopic order as a function of Pe and ϕ and for a fixed particle stiffness $\tilde{k}$. First we compute the global hexatic order parameter $\psi_6 = \langle |\frac{1}{N} \sum_{i=1}^{N} \phi_{6i}| \rangle$. Here $\phi_{6i} = \frac{1}{N_b} \sum_{j \in N_b} e^{6i\theta_{ij}}$, quantifies the local hexatic order in the system. Here θ_{ij} is the angle between the distance vector $\mathbf{r}_{ij}$ and the reference axis, and N_b is the total number of neighbors for a particle i obtained by Voronoi tessellation. Next, we also calculate the largest cluster fraction $f_L = \langle C_m \rangle / N$, where C_m is the number of particles in the largest cluster. Here a pair of particles i and j forms a cluster if $r_{ij} < \sigma$.

A. Phase behavior

The results are shown in Fig. 1 for $\tilde{k} = 2000$. In the phase diagram [Fig. 1(a)], the color map indicate the global hexatic order (ψ_6). The dotted lines represent the contours for $f_L = 0.2, 0.4$, and 0.6 which demarcate the parameter range where large clusters are formed. In the case of MIPS, $\psi_6 \approx 1$ and $f_L > 0.6$ as evident in Fig. 1(a) (for example, point B). Interestingly, there also exists a well-defined region in the phase diagram with large f_L and small ψ_6—for example points A and C in Fig. 1(a). The structural properties in these regions are quite different from MIPS as evident from Figs. 1(b)–1(d), where the typical configurations of the largest cluster at the steady states are plotted. While both regions A and C show a porous structure similar to a percolated state, region B shows a single dense state as usually seen in MIPS. To further confirm the structural difference between these regions, we overlay the local hexatic order ϕ_{6i} on the steady-state full configuration as shown in Figs. 1(e)–1(g). While region B shows large ϕ_{6i} within the dense phase [Fig. 1(f)] which is a signature of MIPS, both regions A and C lack this property. However, unlike region C, region A shows small patches of large ϕ_{6i} values due to the formation of local clusters. Note that the origins of these two states are different. The porous cluster seen in region A is due to an increase in the contact probability caused by low but nonzero motility and occurs with minimal particle overlap. On the other hand, the high-motility porous clusters in region C appears after the breakdown of MIPS with enhanced particle overlap (see Fig. 5). This difference
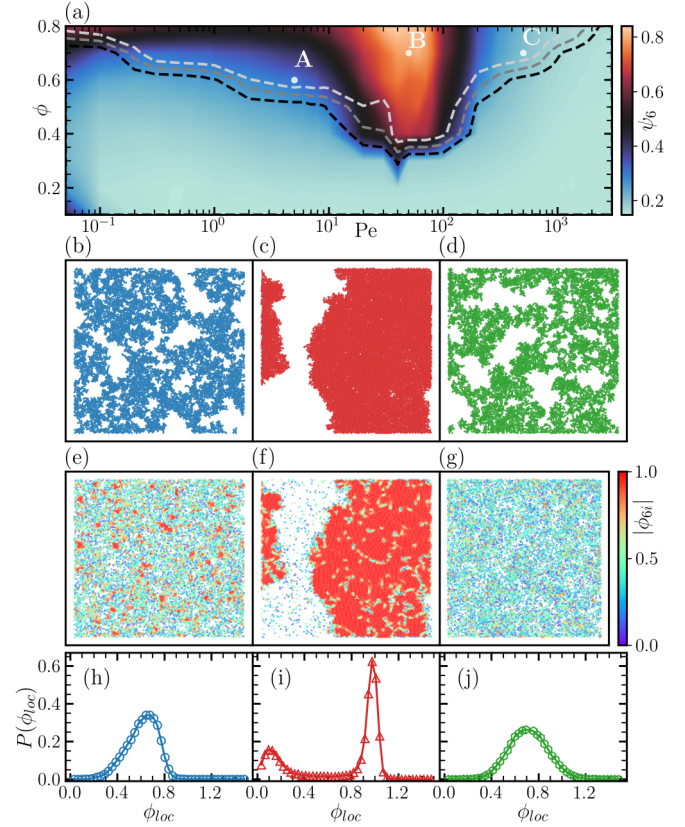

FIG. 1. (a) Contour map of the hexatic order parameter ψ_6 in the (Pe-ϕ) plane. The dotted lines indicate the parameters for which mean largest cluster fraction f_L has values 0.2 (black), 0.4 (gray), and 0.6 (white). A $\equiv (5, 0.6)$, B $\equiv (50, 0.7)$, and C $\equiv (300, 0.7)$ are three representative points in the (Pe-ϕ) plane whose phase properties are further compared. [(b)–(d)] Steady-state configuration of the largest cluster at the locations A, B, and C respectively. [(e) and (f)] The corresponding steady-state snapshots for the complete system. Color code of the particles represents the local hexatic order ϕ_{6i}. [(h)–(j)] Corresponding distribution of the local density ϕ_{loc}. For our simulations we used $N = 10^4$ particles. The stiffness parameter $\tilde{k} = 2000$ for all the figures.

between A and C is further evident in Figs. 1(h) and 1(j) where we plot local density distribution $P(\phi_{\text{loc}})$. While $P(\phi_{\text{loc}})$ for both regions A and C are unimodal, the distribution in region A [see Fig. 1(h)] is clearly assymmetric. This asymmetry in the distribution is a reflection of limitation of the system to form dense local regions, due to low motility. Thus, it is evident that these two porous regions are distinct at the level of local structure. We later show that the porous structure at low Pe [Fig. 1(b)] is an exceptional feature and disappears in the presence of translational thermal noise. The local density distribution for region B displays a bimodal behavior [Fig. 1(i)] as expected from a MIPS state [43].

B. Analysis of transitions

It is evident from Fig. 1 that the system goes through multiple transitions at large ϕ with increase in Pe. Furthermore the porous structures formed at both high and low Pe are
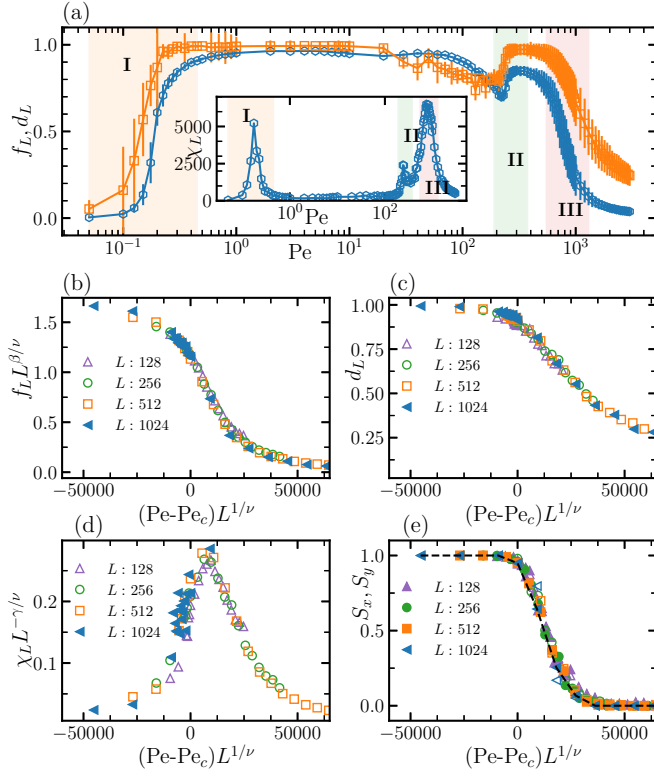
FIG. 2. (a) Semilog plot of the mean largest cluster fraction f_L and the average linear extension of the largest cluster d_L, and susceptibility χ_L (inset) as a function of the Pe at a constant $\phi = 0.7$. Regions I, II, and III indicate different transition regions. Panels (b)–(d) showed the finite-size scaling of order parameter (b)f_L, (c) d_L, (d) χ_L, and (e) the spanning probabilities S_x and S_y with system size $L = 128, 256, 512, 1024$. The collapse occurs for exponent values $\nu \approx 1.33$, $\beta \approx 0.14$, and $\gamma \approx 2.5$. $\mathrm{Pe}_c \approx 550$ as estimated from the fourth-order Binder cumulant.

reminiscent of a percolated state. For a closer analysis, we fix the density at $\phi = 0.7$ and study the system properties with Pe. In addition to f_L, we also calculate the normalized average linear extension of the largest cluster d_L [see Fig. 2(a)] [55]. For low Pe [region I in Fig. 2(a)], both f_L and d_L increases from zero around Pe ≈ 0.5, indicating the formation of a large space-filling cluster. This initial increase in both f_L (and d_L) at small Pe is mainly due to an increase in probability of the particles to make contact with its neighbors as the particle becomes motile. However, in the presence of a translational noise, this cluster formation shifts to a higher Pe (see Fig. 10). On further increasing Pe, we obtain a MIPS state around Pe ≈ 20. Note that f_L does not capture this transition since its value is already large; however d_L shows a decrease from its maximum value 1, since the cluster is no longer space-filling. Interestingly, at even larger Pe (Pe $\gtrsim 100$), both f_L and d_L start to decrease until they reach a minimum around Pe ≈ 200, indicating a reduction in cluster size. Both f_L and d_L again reaches a broad maximum around Pe ≈ 400 beyond which it starts to decrease again. These changes in f_L, marked as regions II and III in Fig. 2(a), indicate structural transitions in the system. To further investigate these possible transitions, we also calculate the susceptibility $\chi_L = L^2 \sigma_L$ as a function

of Pe [see inset of Fig. 2(a)], where $\sigma_L = \sqrt{\langle (f_L - \langle f_L \rangle^2) \rangle}$ is second cumulant. We see clear peaks in χ_L in regions I and III, whereas in region II the peak amplitude is relatively small.

The peaks in χ_L is an indication of phase transitions at these regions and each of these transitions corresponds to a structural change (see Fig. 6). The first transition (region I) corresponds to a change from a state with $f_L \approx 0$ to another state with $f_L \approx 1$ where the system forms a porous, space-filling cluster [see Figs. 1(b) and 1(e)]. Around Pe ≈ 20, the system goes through a structural transition to a MIPS state [see Fig. 9(a)]. After the MIPS transition, there is a gradual increase in the local density within the dense cluster with Pe [see Fig. 9(a)], indicating an overall decrease in the cluster area. There is also a systematic increase in the number of defects and an overall decrease in the global hexatic order [see Fig. 9(b)–8(d)]. Around Pe ≈ 300, the MIPS state dissolves into a porous, space-filling cluster [Fig. 9(a)]. The observed dip in f_L and peak in χ_L in region II is associated with this structural change. Further increase in Pe leads to yet another structural transition at Pe > 1000, where the space-filling cluster breaks up into a large number of smaller clusters. A peak in χ_L at region III captures this transition. To test the robustness of the transitions, we have also studied the system in the presence of translational noise of thermal origin. This is characterized an additional noise term $\xi_i(t)$ in Eq. (C1), such that $\langle \xi_i(t)\xi_j(t') \rangle = 2 D \delta_{ij} \delta(t - t')$, where $D = \frac{\sigma^2 D_r}{3}$. We note that the transition captured by f_L and χ_L at low Pe disappears completely, while the transition to MIPS state is now clearly identified (see Fig. 10). The transitions at high Pe beyond MIPS (II and III), however, remain unaffected (see Fig. 10). This clearly indicates that while the transition at low Pe is also a function of temperature, the transitions seen beyond MIPS are purely dependent on the interplay of the strength of the nonequilibrium forces and the interaction softness.

The transition in region III is particularly interesting as it shows the traits of a conventional percolation transition over a wide range of Pe and is robust to thermal fluctuations. To verify the existence of a percolation transition, we also calculate the spanning probability of the largest cluster, S_x and S_y in both x and y directions respectively. We further perform a finite-size scaling for $L = 128, 256, 512$, and 1024. For a standard percolation transition, the order parameter f_L and the susceptibility χ_L should satisfy the scaling relations $f_L = L^{-\beta/\nu} f((\mathrm{Pe} - \mathrm{Pe}_c)L^{1/\nu})$ and $\chi_L = L^{-\gamma/\nu} g((\mathrm{Pe} - \mathrm{Pe}_c)L^{1/\nu})$, respectively [56]. Here Pe_c is the critical parameter value at the transition point, and β, ν, and γ are the universal exponents. To determine the Pe_c we calculate the fourth-order Binder cumulant $U_L = \frac{1}{2} \left(3 - \frac{\langle d_L^4 \rangle}{\langle d_L^2 \rangle^2} \right)$ for different L and find that the crossing point is at $\mathrm{Pe}_c \approx 550$ (see Fig. 8). Using this Pe_c we scale f_L, d_L, and χ_L, and $S_{x/y}$ values and find a good collapse with L, for the exponents $\nu \approx 1.33$, $\beta \approx 0.14$, and $\gamma \approx 2.5$ [see Figs. 2(b)–2(d)]. These critical exponents are in good agreement with the known universal exponents for standard 2D percolation [57]. We also quantified the error in the estimation of Pe_c value which was $\lesssim 5\%$. Thus, the scaling of the measured quantities and the values of the critical exponents confirms that the transition in region III is indeed a percolation transition.
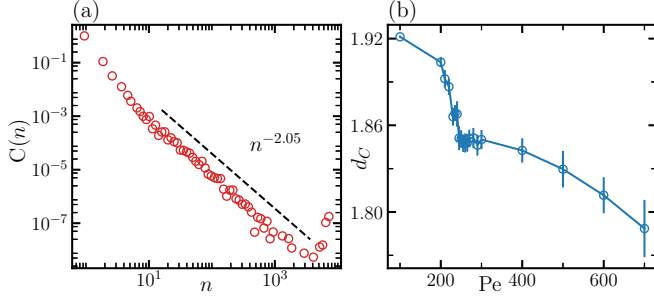
FIG. 3. (a) Cluster size distribution $C(n)$ at Pe = 550 showing a power-law decay with exponent $\tau \approx -2.05$. (b) Correlation dimension (d_C), measured inside the largest cluster for systems with $f_L > 0.4$, as a function of Pe.

Percolation transitions are also associated with a scale-free size distribution of the clusters. We therefore calculate the cluster-size distribution $C(n)$ near the transition point in region III. As shown in Fig. 3(a), we see a clear power-law behavior, extending over several decades of length scale. We find that $C(n) \sim n^{-\tau}$, where $\tau \approx 2.05$. This value is also consistent with the predictions for percolation transitions in 2D [56,57]. Note that the peak seen at large n is due to finite system size which scales as N (see Fig. 11).

We also quantify the porosity of the clusters at high-Pe regions (Pe $\geqslant$ 100) by calculating the correlation dimension (d_C) of the largest cluster [58–60]. The correlation dimension (d_C), being closely related to the fractal dimension [60], provides the information of the change in porosity of the largest cluster with change in particle motility. At Pe $\approx$ 100, the system has already formed a dense cluster due to MIPS where we obtain $d_C \approx 1.95$. On increasing the Pe, the MIPS cluster in the MIPS state becomes porous near its surface, leading to a sharp decrease in d_C, as shown in Fig. 3(b). With further increase in Pe its internal structure becomes porous, which leads to a monotonic decrease in d_C.

C. Effect of interaction softness

Finally, we study the effect of interaction softness on the phase properties by varying the stiffness constant $\tilde{k}$ keeping Pe constant. In Fig. 4 we plot f_L and χ_L (inset) as a function
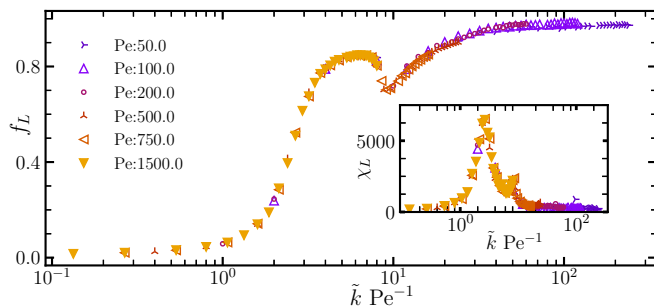

FIG. 4. The largest cluster fraction f_L as a function of stiffness parameter $\tilde{k}$ for different Pe values. Scaling the $\tilde{k}$ axis with Pe^{-1} causes the data to collapse into a single curve. The corresponding scaling for susceptibility (χ_L) is shown in the inset.

of $\tilde{k}$ for different values of Pe. Interestingly, the transitions observed earlier in region II and III, with variation of Pe, are seen here as well but in the reverse order, when $\tilde{k}$ is increased. For each Pe we also see the formation of MIPS when $\tilde{k}$ is sufficiently large. Interestingly, when we scale the $\tilde{k}$ axis with Pe^{-1}, the f_L plots for different Pe collapse to a single curve (see Fig. 4). The same scaling applies for χ_L as shown in the inset of Fig. 4. A similar scaling also applies for the f_L vs Pe curve for different $\tilde{k}$ values, as expected (see Fig. 12). Thus it is evident that an increase in Pe effectively makes the interparticle interactions softer and an increase in motility is equivalent to decreasing the interaction stiffness. This scaling behavior can be further understood in terms of the effective distance r_0 between the particles [61]. When $\tilde{k}$ is decreased, the softening of interaction will lead to a linear decrease in r_0. We numerically estimate r_0 for different Pe from the distribution of interparticle distances r_{ij} for pairs of interacting particles. The computed values of r_0 shows that in the limit of both high and low Pe, an increase in Pe will also cause a similar linear decrease in r_0 [see Fig. 13(c)]. Within the MIPS phase (Pe$\tilde{k}^{-1} \ll 1$), an approximate estimate shows that this linear dependence is of the form $r_0 \approx [1 - (C\tilde{k})^{-1} \text{Pe}]$, ($C$ is a constant, see Appendix F) [61]. We also calculate the cutoff distance r_c below which $p(r_{ij})$ is negligible (see Appendix F). We find that r_c also follows a similar linear decrease with Pe, similarly to r_0, in both high- and low-Pe limits [Fig. 13(c)]. We also note that even for Pe $\approx$ 2Pe$_c$ there is a significant nonzero excluded distance for a pair of interacting particles as verified directly from the simulations, indicating that the particles do not pass through each other in region III.

IV. SUMMARY AND OUTLOOK

In summary, we show that the softness plays a crucial role in determining the phase behavior of active particles, which appears to be much richer than what was conceived so far. It was believed that the ordered state of active Brownian particles with short-ranged repulsive interactions is relatively simple, where an increase in particle motility leads to a density ordering in the system and the destruction of this ordered state was attributed to particle crossing [51]. However, other active matter systems with orientational ordering have shown more complex density effects, such as coarsening [62] and percolation transitions [55]. Here we have shown that complex structural effects can also be observed in systems without orientational ordering, purely driven by high particle motility and softness.

We have characterized the transition at high motility, by combining multiple quantities, namely the mean largest cluster fraction f_L, the linear extension of the largest cluster d_L, the susceptibility χ_L, and spanning probabilities $S_{x/y}$. We performed finite-size scaling of these quantities to confirm that the transition is a standard percolation transition.

We have shown that during this particular transition, motility acts as an effective softness parameter and the structural properties can be scaled with Pe^{-1}. Therefore, the structural transitions that we observe is a softness induced one. When Pe is small, there exists another porous state, which disappears in the presence of translational noise. This porous network,
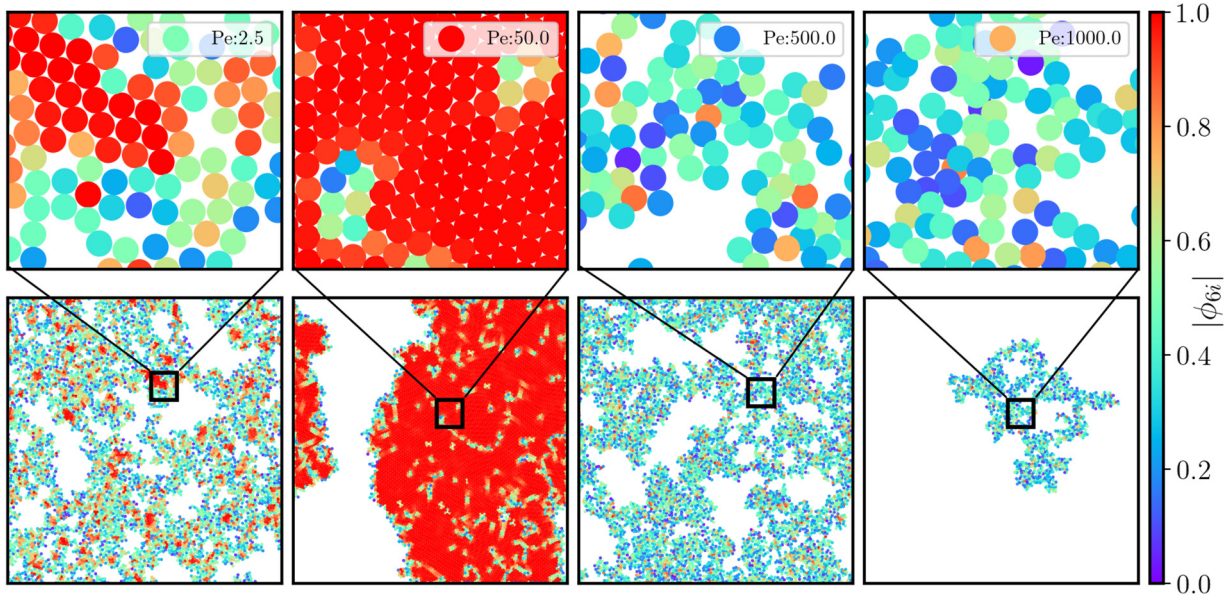
FIG. 5. Plots of steady-state configurations for the entire system at different Pe values of 2.5, 50.0, 500.0, and 1000.0, as well as plots zoomed in on small sections; the color of each particle shows the value of the local hexatic order $|\phi_{6i}|$

unlike the percolated structure at large Pe, has small domains of high local hexatic order.

We note that the specific scaling form, $\mathrm{Pe}^{-1}\tilde{k}$, is a consequence of the harmonic interaction potential, causing a linear decrease in minimum interparticle distance within the clusters, with increase in motility. Deviations from this scaling form are expected if a different form of interaction potential is used, e.g., in many earlier studies, the potential diverges as $r \to 0$ [22,43,61]. Although we use a nondiverging potential, we observe that finite excluded region for interparticle distances vanishes only at very high motility (Pe > Pe$_c$). Thus, we believe that the percolation transition observed at high motility is possibly a generic feature of active particles with soft interaction. However, these results are relevant for systems with rare particle crossings such as cells in tissues. Thus, we show that when we go beyond the idealized hard-particle interactions, new collective properties can arise in active Brownian systems. These findings are particularly important, since most of the natural systems does not consist of hard particles. Our study is also relevant in the context of recent interests in self-assembly of soft colloidal particles [54].

APPENDIX A: COMPARISON OF DIFFERENT STRUCTURE

In Fig. 1 in the manuscript, we have compared the different phase space behavior, particularly the differences of the porous networks at high and low motility, as their difference with MIPS. Here we zoom into small scales to compare the structural differences. This is shown in Fig. 5.

APPENDIX B: DETAILED ANALYSIS OF TRANSITIONS

We analyze the phase behavior of active Brownian particles by calculating various order parameters, averaged at the steady state. The fraction of largest cluster f_L is one of the order parameters that can be used to detect the transitions. In Fig. 6, we show the configuration plots for various Pe for fixed $\phi = 0.7$, where the particles included in the largest clusters are marked separately. The corresponding susceptibility, which is defined for a system with size L, as $\chi_L = L^2 \sigma_L$, where σ_L is the second cumulant of f_L diverges at the transition [see inset of Fig. 2(a) in main text]. Different transitional regions are plotted separately in Fig. 7. A reliable quantity that can be used to estimate transitions is the fourth-order Binder cumulant for different system sizes L. The fourth-order Binder cumulant $U_L = \frac{1}{2}\left(3 - \frac{\langle d_L^4 \rangle}{\langle d_L^2 \rangle^2}\right)$ is calculated for the order parameter d_L which is the normalized maximum linear extension of the largest cluster. The crossing point of U_L for different L provides Pe$_c \approx 550$ (Fig. 8).

However, these order parameters are not helpful in identifying the phase-separated region, which has been visually identified for $20 \gtrsim \mathrm{Pe} \gtrsim 200$. To identify this state more quantitatively, we measure the local density ϕ_{loc} which shows a bimodal distribution when the system phase separates. In Fig. 9 we plot the location of peak values $\phi_{\mathrm{loc}}^{\max}$ of the distribution. This quantity is multivalued in the phase-separated region, hence an indicator for MIPS.

APPENDIX C: THE EFFECT OF TRANSLATIONAL NOISE

In the original dynamical equation for the particle positions [Eq. (1) in the main text] the translational noise is
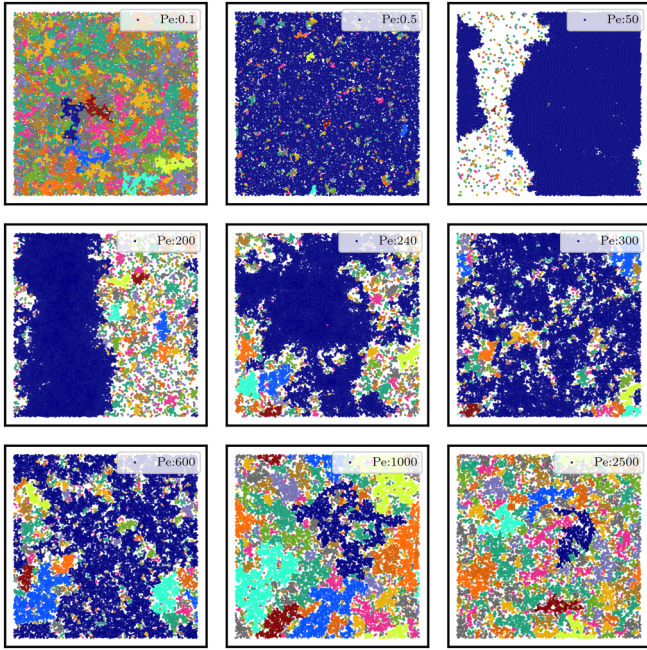
FIG. 6. Cluster distribution for Pe = 0.1, 0.5, 50, 200, 240, 300, 600, 1000, 2500. Color code blue indicates the largest cluster, and other colors represent the rest of the connected clusters. Due to a large number of various clusters, each color is used for several separate clusters.
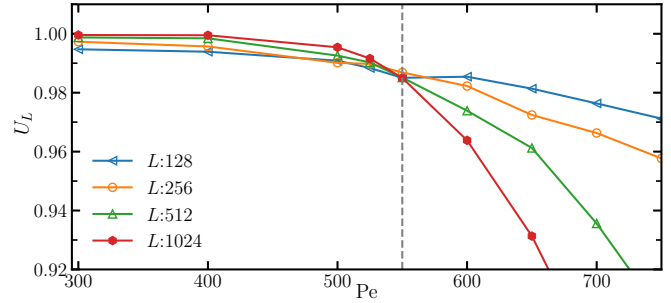

FIG. 8. The fourth-order Binder cumulant U_L is plotted as a function of Pe for four different systems sizes. The curves crosses at Pe $\simeq$ 550.
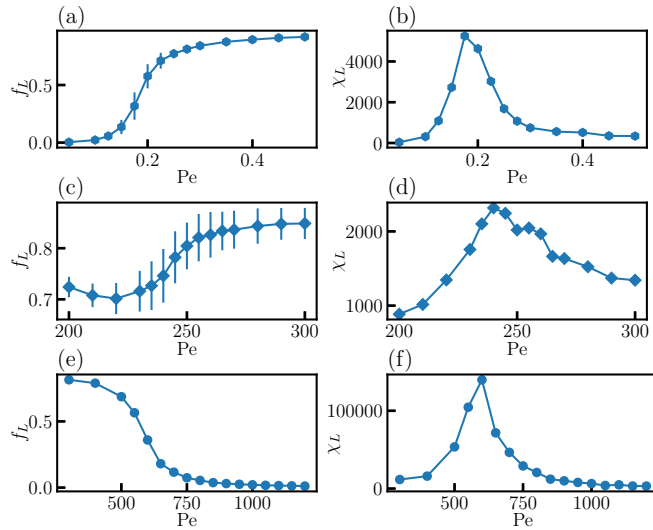

FIG. 7. Three transitions captured by the order parameter cluster fraction f_L at fixed $\phi = 0.7$. Here we show three regions in Pe, I (0.05–0.5), II (200–300), and III (550–1200) as shown in Fig. 2(a) in main text separately. (a) The f_L of the region I show the transition from a homogeneous region with small clusters to the largest connected cluster that spans the whole system as shown in its second cumulant plot (b). Panels (c) and (d) show the transition from MIPS to a percolated cluster of region II for box size $L = 210$. Similarly, [(f) and (g)] region III shows the percolation transition for box size $L = 1024$.
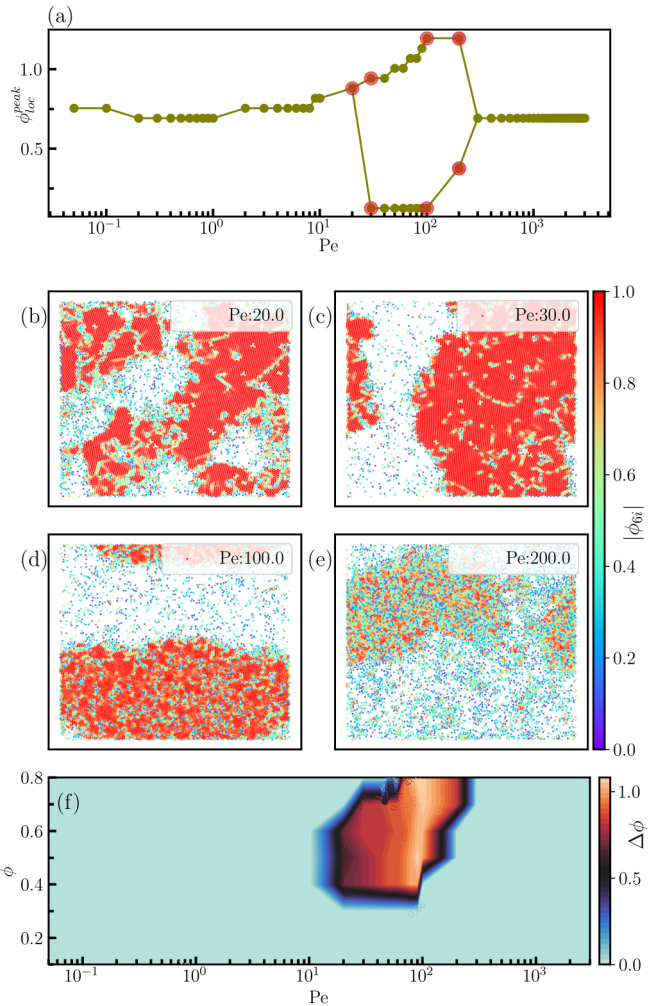

FIG. 9. MIPS: (a) The density corresponding to peak value of the local density distribution is plotted as a function of Pe at fixed $\phi = 0.7$. Panels (b)–(e) are system configuration plots for the four distinct points Pe = 20, 50, 100, 200 here color shows the value of local hexatic order $|\phi_{6i}|$ superimposed on particle configurations. (f) Phase diagram of the density difference $\Delta\phi = \phi_{\text{loc}}^{\text{peak}}(\text{max}) - \phi_{\text{loc}}^{\text{peak}}(\text{min})$ between the dense and dilute regions [as shown in (a)] in the Pe-ϕ plane. A large $\Delta\phi$ indicates MIPS.
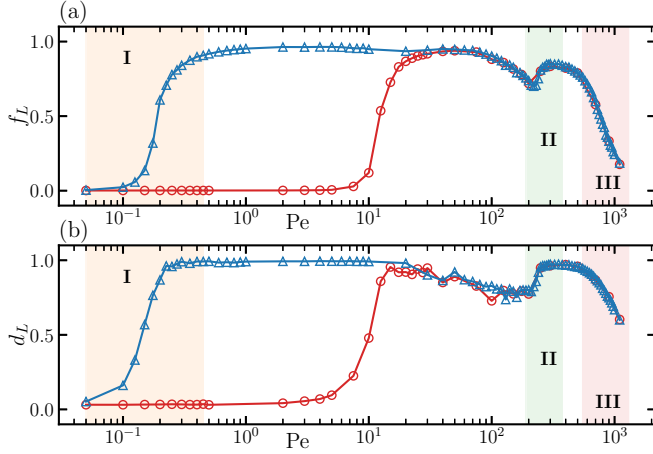
FIG. 10. Comparing system with and without translational diffusion: (a) Mean largest cluster fraction f_L as a function of the Pe at a constant $\phi = 0.7$ (b) normalized average linear extension d_L as a function of Pe. In these plots blue curve represents the system without translational noise D_t and red curve for system with D_t and these are divided into three separate regions in Pe, I (0.05 − 0.5), II (200 − 300), and III (550 − 1100) corresponding to different transition regions as shown in Fig. 2(a) of main text and Fig. 6 of SI.

not included. Although the effect of noise is expected to be negligible in the limit of large motility, it might influence the overall structural properties at low Pe. To study this effect, we run the simulations with an additional noise term to Eq. (1),

$$\dot{\mathbf{r}}_i = \mu \sum_j \mathbf{F}(\mathbf{r}_{ij}) + v_p \hat{\mathbf{n}}_i + \xi_i, \tag{C1}$$

where ξ_i is the noise term which follows the relation $\langle \xi_i(t)\,\xi_j(t')\rangle = 2\,D\delta_{ij}\,\delta(t - t')$ and $\langle \xi_i \rangle = 0$. Here we choose $D = \frac{\sigma^2 D_r}{3}$. The structural properties of this system is analyzed by calculating f_L and d_L as a function of Pe, for $\phi = 0.7$. In Fig. 10, we compare these quantities with and without translational noise. Both f_L and d_L are almost same in both cases at large Pe (Pe $\gtrsim 20$) beyond the MIPS region. However, at low Pe both f_L and d_L are qualitatively different compared to the athermal case. In the presence of noise, we no longer observe the formation of porous clusters at low Pe.

APPENDIX D: FINITE-SIZED EFFECT IN THE CLUSTER SIZE DISTRIBUTION

In Fig. 3(a) of the maintext, we see a peak at large n. This peak is a manifestation of finite system size. To verify this, we have now plotted together the cluster size distribution for three different system sizes, namely $L = 256,\ 512,$ and 1024 [see Fig. 11(a)]. As can be seen clearly, the peak gets shifted to larger n values as L is increased, while the power-law exponent remains unchanged. We also show in Fig. 11(b) that if the x axis is scaled by $L^2 \propto N$, the large cluster-size peaks collapses.

APPENDIX E: EFFECT OF INTERACTION SOFTNESS

The results in Fig. 2 in the main text shows the system behavior for a fixed value of the stiffness parameter, $\tilde{k} = 2000$.
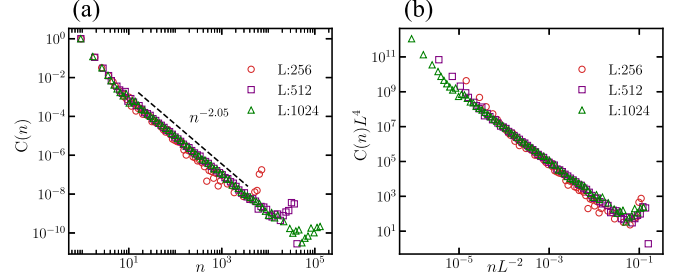

FIG. 11. (a) Cluster size distribution plot for our study shown for three different system sizes, namely $L = 256$, 512, and 1024. (b) The x axis scaled by L^{-2} to show the system size dependence.

Here we systematically study the effect of $\tilde{k}$ in f_L as a function of Pe [Fig. 12(a)]. It is clear that at low Pe (Pe $\lesssim 20$) the change in $\tilde{k}$ does not have a significant influence in f_L. However, where Pe $\gtrsim 20$, the interparticle interaction becomes crucial and we observe a systematic shift in the values of f_L to higher Pe, when $\tilde{k}$ is increased. As expected, we these data points collapse by scaling the x axis with $\tilde{k}^{-1}$ [Fig. 12(b)].

APPENDIX F: CALCULATION OF PEAK AND CUTOFF INTERPARTICLE DISTANCES

An increase in interaction softness is manifested as a decrease in interparticle distance between a pair of interacting particles. To quantify this, we calculate the distribution of interparticle distances $p(r_{ij})$ between a pair of particles within the largest cluster. As shown in Fig. 13(a), the distribution has a maximum at $r_{ij} \lesssim \sigma$. For a given stiffness ($\tilde{k} = 2000$), we find that the width of the distribution increases while the peak value (r_{peak}) shifts only marginally [Figs. 13(a) and 13(b)], especially for Pe > 300 where the MIPS state is destroyed. This increase in width indicates a deviation from the hexatic crystalline order and a higher degree of disorder within the cluster. We define the cutoff distance r_c as the separation at which $p(r_{ij})$ decays into one percent of its maximum value at $r_{ij} = r_{\text{peak}}$. We plot r_c as a function of Pe [see Fig. 13(c)] and observe a linear decrease with Pe in the limit of both high and low values of Pe. The cutoff r_c has a significant nonzero value even for very high motility as evident in Figs. 13(a) and 13(c). Further, we did not observe a single event with $r_{ij} \leqslant 0.2$
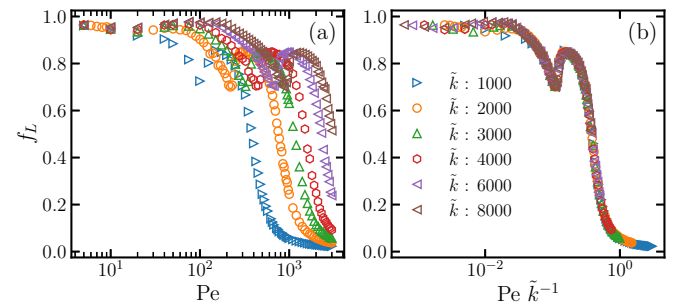

FIG. 12. (a) f_L plotted as a function of Pe for different values of $\tilde{k}$. For Pe < 20 the f_L values are overlapping for all $\tilde{k}$. However, there is a shift toward higher Pe with increase in $\tilde{k}$, for Pe > 20. (b) The scaling of Pe with $\tilde{k}^{-1}$ collapses f_L.
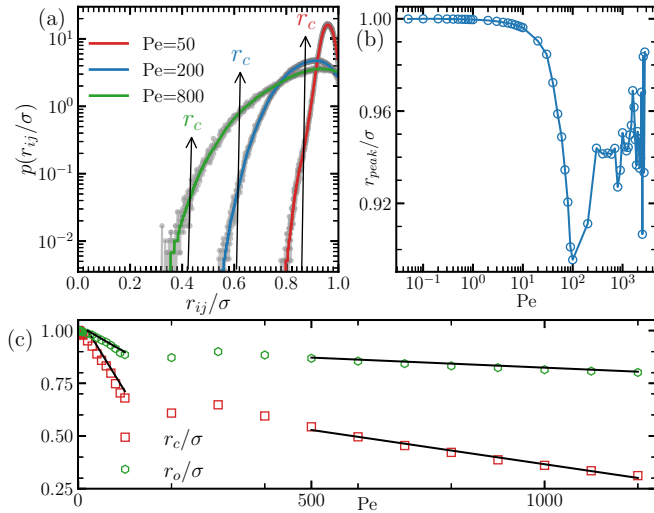
FIG. 13. (a) Interparticle distance distribution for Pe = 50, 200, and 800, where r_c/σ is cut off distance for which $p(r_{ij}/\sigma)$ is 1% of the peak value. (b) Semilog plot of r_{peak}/σ as a function of Pe. (c) r_c/σ and r_0/σ plotted as a function of Pe. Black lines shows the corresponding linear fits.

for $\tilde{k} = 2000$ even for Pe = 2Pe$_c$. These observations verify that despite the interaction softness, the particles do not pass through each other in the high-motility percolated state and there exists a lower cutoff for r_{ij} below which the particles do not approach (Fig. 5).

We also plot the average interparticle distance r_0, calculated from the numerical data. Similar to r_c, r_0 also shows a linear decrease in both low- and high-Pe limits [Fig. 13(c)]. An approximate theoretical estimation of the average interparticle distance r_0 can be made within the MIPS state [61], which is given as

$$r_0 \approx \frac{1}{2}\left[1 + \sqrt{1 - \frac{4}{C}\left(\frac{\text{Pe}}{\tilde{k}}\right)}\right].$$

We note that within the MIPS region, since $(\text{Pe}/\tilde{k}) \ll 1$, r_0 also follows a linear relation, $r_0 \approx 1 - \frac{1}{C}(\frac{\text{Pe}}{\tilde{k}})$. Taking $C \approx 0.39$, our estimate for r_0 within the MIPS state is in qualitative agreement with the data [see Fig. 13(c)].

Interestingly, after the percolation transition, both r_c and r_0 within the largest cluster still scales linearly [$r_c \sim -0.65\tilde{k}^{-1}$ Pe and $r_0 \sim -0.19\tilde{k}^{-1}$ Pe, see Fig. 13(c)]. The behaviors of both r_c and r_0 are consistent with the scaling used to collapse the data in Fig. 4 in the maintext. This behavior explains the overall linear scaling of f_L and χ_L with $\tilde{k}\text{Pe}^{-1}$ in Fig. 12 and Fig. 4 in the main text. We note that this linear decrease in r_c is likely to be consequence of the particular form of the interaction. Many of the previous studies on ABPs have used interaction potentials which diverge as $\frac{1}{r_{ij}^\alpha}$, where $\alpha > 1$. In such cases the scaling of r_c with Pe is expected to be different. However, since the overall physical properties are determined by the overlap distance, we believe that the percolation transition at high Pe (or high softness) will be observed for sufficiently large motilities, irrespective of the form of interparticle interactions.

[1] S. Ramaswamy, Annu. Rev. Condens. Matter Phys. **1**, 323 (2010).

[2] T. Vicsek and A. Zafeiris, Phys. Rep. **517**, 71 (2012).

[3] M. C. Marchetti, J. F. Joanny, S. Ramaswamy, T. B. Liverpool, J. Prost, M. Rao, and R. A. Simha, Rev. Mod. Phys. **85**, 1143 (2013).

[4] A. Cavagna, A. Cimarelli, I. Giardina, G. Parisi, R. Santagati, F. Stefanini, and M. Viale, Proc. Natl. Acad. Sci. USA **107**, 11865 (2010).

[5] C. Becco, N. Vandewalle, J. Delcourt, and P. Poncin, Physica A **367**, 487 (2006).

[6] H.-P. Zhang, A. Be'er, E.-L. Florin, and H. L. Swinney, Proc. Natl. Acad. Sci. USA **107**, 13626 (2010).

[7] A. Be'er, B. Ilkanaiv, R. Gross, D. B. Kearns, S. Heidenreich, M. Bär, and G. Ariel, Commun. Phys. **3**, 66 (2020).

[8] T. H. Tan, J. Liu, P. W. Miller, M. Tekant, J. Dunkel, and N. Fakhri, Nat. Phys. **16**, 657 (2020).

[9] F. Julicher, K. Kruse, J. Prost, and J.-F. Joanny, Phys. Rep. **449**, 3 (2007), nonequilibrium physics: From complex fluids to biological systems III. Living systems.

[10] V. Schaller, C. Weber, C. Semmrich, E. Frey, and A. R. Bausch, Nature (London) **467**, 73 (2010).

[11] Y. Sumino, K. H. Nagai, Y. Shitaka, D. Tanaka, K. Yoshikawa, H. Chaté, and K. Oiwa, Nature (London) **483**, 448 (2012).

[12] M. Rubenstein, A. Cornejo, and R. Nagpal, Science **345**, 795 (2014).

[13] G. Kokot, S. Das, R. G. Winkler, G. Gompper, I. S. Aranson, and A. Snezhko, Proc. Natl. Acad. Sci. USA **114**, 12870 (2017).

[14] J. A. Cohen and R. Golestanian, Phys. Rev. Lett. **112**, 068302 (2014).

[15] G. Gompper, R. G. Winkler, T. Speck, A. Solon, C. Nardini, F. Peruani, H. Löwen, R. Golestanian, U. B. Kaupp, L. Alvarez *et al.*, J. Phys.: Condens. Matter **32**, 193001 (2020).

[16] A. Bricard, J.-B. Caussin, N. Desreumaux, O. Dauchot, and D. Bartolo, Nature (Lond.) **503**, 95 (2013).

[17] S. Thutupalli, R. Seemann, and S. Herminghaus, New J. Phys. **13**, 073021 (2011).

[18] I. Buttinoni, J. Bialké, F. Kümmel, H. Löwen, C. Bechinger, and T. Speck, Phys. Rev. Lett. **110**, 238301 (2013).

[19] M. N. van der Linden, L. C. Alexander, D. G. A. L. Aarts, and O. Dauchot, Phys. Rev. Lett. **123**, 098001 (2019).

[20] A. Wysocki, R. G. Winkler, and G. Gompper, Europhys. Lett. **105**, 48004 (2014).

[21] M. E. Cates and J. Tailleur, Annu. Rev. Condens. Matter Phys. **6**, 219 (2015).

[22] P. Digregorio, D. Levis, A. Suma, L. F. Cugliandolo, G. Gonnella, and I. Pagonabarraga, Phys. Rev. Lett. **121**, 098003 (2018).

[23] C. B. Caporusso, P. Digregorio, D. Levis, L. F. Cugliandolo, and G. Gonnella, Phys. Rev. Lett. **125**, 178004 (2020).

[24] J. Stenhammar, A. Tiribocchi, R. J. Allen, D. Marenduzzo, and M. E. Cates, Phys. Rev. Lett. **111**, 145702 (2013).

[25] D. Levis, J. Codina, and I. Pagonabarraga, Soft Matter **13**, 8113 (2017).

[26] J. U. Klamser, S. C. Kapfer, and W. Krauth, Nat. Commun. **9**, 5045 (2018).

[27] S. Mandal, B. Liebchen, and H. Löwen, Phys. Rev. Lett. **123**, 228001 (2019).

[28] L. Caprini, U. Marini Bettolo Marconi, and A. Puglisi, Phys. Rev. Lett. **124**, 078001 (2020).

[29] S. Das and R. Chelakkot, Soft Matter **16**, 7250 (2020).

[30] C. F. Lee, New J. Phys. **15**, 055007 (2013).

[31] Y. Fily, A. Baskaran, and M. F. Hagan, Soft Matter **10**, 5609 (2014).

[32] J. Elgeti and G. Gompper, Europhys. Lett. **101**, 48003 (2013).

[33] X.-q. Shi, G. Fausti, H. Chaté, C. Nardini, and A. Solon, Phys. Rev. Lett. **125**, 168001 (2020).

[34] J. Su, H. Jiang, and Z. Hou, New J. Phys. **23**, 013005 (2021).

[35] J. Stenhammar, D. Marenduzzo, R. J. Allen, and M. E. Cates, Soft Matter **10**, 1489 (2014).

[36] M. R. Shaebani, A. Wysocki, R. G. Winkler, G. Gompper, and H. Rieger, Nat. Rev. Phys. **2**, 181 (2020).

[37] T. Vicsek, A. Czirók, E. Ben-Jacob, I. Cohen, and O. Shochet, Phys. Rev. Lett. **75**, 1226 (1995).

[38] F. Peruani, T. Klauss, A. Deutsch, and A. Voss-Boehme, Phys. Rev. Lett. **106**, 128101 (2011).

[39] F. Ginelli and H. Chaté, Phys. Rev. Lett. **105**, 168103 (2010).

[40] H. Chaté, F. Ginelli, G. Grégoire, F. Peruani, and F. Raynaud, Eur. Phys. J. B **64**, 451 (2008).

[41] H. Chaté, F. Ginelli, and R. Montagne, Phys. Rev. Lett. **96**, 180602 (2006).

[42] Y. Fily and M. C. Marchetti, Phys. Rev. Lett. **108**, 235702 (2012).

[43] G. S. Redner, M. F. Hagan, and A. Baskaran, Phys. Rev. Lett. **110**, 055701 (2013).

[44] T. Speck, A. M. Menzel, J. Bialké, and H. Löwen, J. Chem. Phys. **142**, 224109 (2015).

[45] G. S. Redner, A. Baskaran, and M. F. Hagan, Phys. Rev. E **88**, 012305 (2013).

[46] S. Paliwal, V. Prymidis, L. Filion, and M. Dijkstra, J. Chem. Phys. **147**, 084902 (2017).

[47] N. A. Söker, S. Auschra, V. Holubec, K. Kroy, and F. Cichos, Phys. Rev. Lett. **126**, 228001 (2021).

[48] Z.-F. Huang, A. M. Menzel, and H. Löwen, Phys. Rev. Lett. **125**, 218002 (2020).

[49] F. Jose, S. K. Anand, and S. P. Singh, Soft Matter **17**, 3153 (2021).

[50] T. Hiraiwa, Phys. Rev. Lett. **125**, 268104 (2020).

[51] Y. Fily, S. Henkes, and M. C. Marchetti, Soft Matter **10**, 2132 (2014).

[52] R. Agrawal and D. A. Kofke, Phys. Rev. Lett. **74**, 122 (1995).

[53] C. Rey, J. Garcia-Rodeja, L. J. Gallego, and M. J. Grimson, Phys. Rev. E **57**, 4420 (1998).

[54] J. Menath, J. Eatson, R. Brilmayer, A. Andrieu-Brunsen, D. M. A. Buzza, and N. Vogel, Proc. Natl. Acad. Sci. USA **118**, e2113394118 (2021).

[55] N. Kyriakopoulos, H. Chaté, and F. Ginelli, Phys. Rev. E **100**, 022606 (2019).

[56] D. Stauffer and A. Aharony, *Introduction to Percolation Theory* (CRC Press, Boca Raton, FL, 2018)

[57] E. T. Gawlinski and H. E. Stanley, J. Phys. A: Math. Gen. **14**, L291 (1981).

[58] P. Grassberger and I. Procaccia, Phys. Rev. Lett. **50**, 346 (1983).

[59] S. Lahmiri, C. Tadj, C. Gargour, and S. Bekiros, Chaos Solitons Fract. **143**, 110639 (2021).

[60] S. H. Strogatz, *Nonlinear Dynamics and Chaos with Student Solutions Manual: With Applications to Physics, Biology, Chemistry, and Engineering* (CRC Press, Boca Raton, FL, 2018).

[61] M. Sanoria, R. Chelakkot, and A. Nandi, Phys. Rev. E **103**, 052605 (2021).

[62] S. Dey, D. Das, and R. Rajesh, Phys. Rev. Lett. **108**, 238001 (2012).